Exchange, correlation, and scattering effects on surface plasmons in arm-chair graphene nanoribbons

M. Bahrami[*], and P. Vasilopoulos

Department of Physics, Concordia University, 7141 Sherbrooke Ouest Montréal, Québec H4B 1R6, Canada
[*]*m_bahra@live.concordia.ca*

Abstract: Using Maxwell's equations for the incoming and outgoing electromagnetic field, in interaction with a metallic arm-chair graphene nanoribbon (AGNR), and the relationship between the density-density response function and the conductivity, we study surface plasmons (SPs) in a AGNR following the Lindhard, random-phase approximation (RPA), and Hubbard approaches. For transverse magnetic (TM) modes we obtain *analytical* dispersion relations (DRs) valid for $q \leq k_F$ and assess their width dependence. In all approaches we include screening. In the long-wavelength limit $q \to 0$ there is a small but noticeable difference between the DRs of the three approaches. In this limit the respective, scattering-free conductivities differ drastically from those obtained when scattering by impurities is included. We demonstrate that the SP field is proportional to the square of the quality factor Q. The reflection amplitude shows that metallic AGNRs do not support Brewster angles. In addition, AGNRs do not support transverse electric (TE) SPs.

References and links

1. D. K. Gramotnev and S. I. Bozhevolnyi, "Plasmonics beyond the diffraction limit," Nature Photonics **4**, 83 - 91 (2010).
2. M. S. Kushwaha, "Plasmons and magnetoplasmons in semiconductor heterostructures," Surf. Sci. Reports. **41**, 1-416 (2001).
3. G. V. Naik, V. M. Shalaev, A. Boltasseva, "Alternative Plasmonic Materials: Beyond Gold and Silver," Advanced Materials **25**, 3264-3294 (2013).
4. E. Ozbay, "Plasmonics: Merging Photonics and Electronics at Nanoscale Dimensions," Science **13**, 189-193 (2006).
5. S. A. Maier, *Plasmonics: fundamentals and applications* (Springer, 2007).
6. T. Low and P. Avouris, "Graphene Plasmonics for Terahertz to Mid-Infrared Applications," ACS Nano. **8**, 1086-1101 (2014).
7. Z. Sun, A. Martinez and F. Wang, "Optical modulators with 2D layered materials," Nature Photonics **10**, 227-238 (2016).
8. S. Jang, E. Hwang, Y. Lee, S. Lee, and J. H. Cho, "Multifunctional Graphene Optoelectronic Devices Capable of Detecting and Storing Photonic Signals," Nano Lett. **15**, 2542-2547 (2015).
9. Y. Zhao and Y. Zhu, "Graphene-based hybrid films for plasmonic sensing," Nanoscale., **7**, 14561-14576 (2015).
10. M. Kauranen and A. V. Zayats, "Nonlinear plasmonics," Nature Photonics **6**, 737-748 (2012).
11. Q. Bao and K. P. Loh, "Graphene Photonics, Plasmonics, and Broadband Optoelectronic Devices," ACS Nano. **2**, 3677-3694 (2012).
12. L. Ju, B. Geng, J. Horng, C. Girit, M. Martin, Z. Hao, H. A. Bechtel, X. Liang, A. Zettl, Y. R. Shen and F. Wang, "Graphene plasmonics for tunable terahertz metamaterials," Nature Nanotechnology **6**, 630-634 (2011).
13. A. A. Shylau, S. M. Badalyan, F. M. Peeters, A. P. Jauho, "Electron polarization function and plasmons in metallic armchair graphene nanoribbons," Phys. Rev. B **91**, 205444 (2015).
14. D. R. Andersen and H. Raza, "Collective modes of massive Dirac fermions in armchair graphene nanoribbons," J. Phys. Condens. Matter **25**, 045303 (2013).
15. L. Brey and H. A. Fertig, "Elementary electronic excitations in graphene nanoribbons," Phys. Rev. B **75**, 125434 (2007).
16. C. E. P. Villegas, M. R. S. Tavares, G. Q. Hai, and P. Vasilopoulos, "Plasmon modes and screening in double metallic armchair graphene nanoribbons," Phys. Rev. B **88**, 165426 (2013).
17. M. Bagheri and M. Bahrami, "Plasmons in spatially separated double-layer graphene nanoribbons," J. Appl. Phys. **115**, 174301 (2014).

18. H. Bruus and K. Flensberg, *Introduction to many-body quantum theory in condensed matter physics* (Oxford University, 2004).

19. Y. Wang and D. R. Andersen, "First-principles study of the terahertz third-order nonlinear response of metallic armchair graphene nanoribbons," Phys. Rev. B **93**, 235430 (2016).

20. Y-W Son, M. L. Cohen, and S. G. Louie, "Energy Gaps in Graphene Nanoribbons," Phys. Rev. Lett. **97**, 216803 (2006); D. Gunlycke and C. T. White, "Tight-binding energy dispersions of armchair-edge graphene nanostrips," Phys. Rev. B **77**, 115116 (2008).

21. G. Seol, and J. Guo, "Bandgap opening in boron nitride confined armchair graphene nanoribbon," Appl. Phys. Lett, **98**, 143107 (2011).

22. G. Z. Magda, X. Jin, I. Hagymasi, P. Vancso, Z. Osvath,, P. Nemes-Incze, C. Hwang, L. P. Biro, and L. Tapaszto, "Room-temperature magnetic order on zigzag edges of narrow graphene nanoribbons," Nature , **514**, 608-611 (2014)

23. F. J. G. Abajo, "Graphene Plasmonics: Challenges and Opportunities," ACS Photonics. **1**, 135-152 (2014).

24. D. N. Basov, M. M. Fogler, A. Lanzara, Feng Wang, Y. Zhang, "Colloquium: Graphene spectroscopy," Rev. Mod. Phys. **86**, 959 (2014).

25. Gradshteyn and Ryzhik, *Tables of integrals, Series, and Products* (Academic, 2014).

26. M. Tas, *Dielectric formulation of one-dimensional electron gas*, 2004.

27. V. N. Kotov, B. Uchoa, V. M. Pereira, F. Guinea, and A. H. Castro Neto, "Electron-Electron Interactions in Graphene: Current Status and Perspectives," Rev. Mod. Phys. **84**, 1067 (2011).

28. B. Wunsch, T. Stauber, F. Sols, and F. Guinea, "Dynamical polarization of graphene at finite doping," New Journal of Physics. **8**, 318 (2006).

29. S. Xiao, X. Zhu, B.H. Li, N. A. Mortensen, "Graphene-plasmon polaritons: From fundamental properties to potential applications," Front. Phys. **11**, 117801 (2016).

30. Y. Zhong, S. D. Malagari, T. Hamilton, and D. Wasserman, "Review of mid-infrared plasmonic materials," Journal of Nanophotonics. **9**, 093791 (2015).

31. T. Stauber, "Plasmonics in Dirac systems: from graphene to topological insulators," Journal of Physics: Cond. Matter. **26**, 123201 (2014).

32. A. N. Grigorenko, M. Polini and K. S. Novoselov, "Graphene plasmonics," Nature Photonics **6**, 749-758 (2012).

33. A. Politano and G. Chiarello, "Plasmon modes in graphene: status and prospect," Nanoscale **6**, 10927-10940 (2014).

34. S. A. Mikhailov and D. Beba, "Nonlinear broadening of the plasmon linewidth in a graphene stripe," New Journal of Physics. **14**, 115024 (2012).

35. W. Wang and J. M. Kinaret, "Plasmons in graphene nanoribbons: Interband transitions and nonlocal effects," Phys. Rev. B **87**, 195424 (2013).

36. J. H. Strait, P. Nene, W. M. Chan, C. Manolatou, S. Tiwari, and F. Rana, "Confined plasmons in graphene microstructures: Experiments and theory," Phys. Rev. B **87**, 241410 (2013).

37. G. F. Giuliani and G. Vignale, *Quantum theory of the electron liquid* (Cambridge University, 2005).

---

1. Introduction

Reducing the size of semiconductor devices, circuits, and components exerts an influence on their performance and speeds up information processes [1, 2]. However, size reduction poses major problems such as short-channel effects, gate leakage, and drastically increasing power density [3]. One successful effective solution is to supersede electromagnetic waves as information carriers [1]. Due to their extremely high bandwidth, fibre-optics communication devices can carry information by three oders of magnitude faster than electronic circuits [4]. Nevertheless, because of diffraction limits, this does not allow to localize the electromagnetic field in regions smaller than half of the wavelength and integrating optical devices and circuits has encountered serious problems [1, 3]. One of the promising solutions is surface plasmons (SPs). SPs are evanescent electromagnetic fields that can propagate along the interface of two media under specific conditions [5] which, however, can be provided by a joint metal-dielectric medium. Due to the SP's evanescent character, the SP wavelength is smaller than that of a free electromagnetic wave. This SP feature plays a pivotal role in many applications, such as integrated photonic systems, biosensing, photovoltaic devices, single-photon transistors for quantum computing, optical modulators, photonic memory devices, surface enhanced Raman spectroscopy [6–9], and boosting nonlinear optical effects [10].

SPs provide extremely fast processing, in the order of a few femtoseconds [10]. Gold and silver as noble metals are predominant materials for plasmonics. However, they suffer from disadvantages such as high ohmic losses and non-tunability [11]. Size reduction of plasmonic

materials give rises to SPs with smaller wavelength. In addition to gold and silver, two-dimensional (2D) plasmonic materials, such as a 2D electron gas (2DEG), polar interfaces of oxides, and oxide nanosheets have more merits than bulk 3D materials. Because of high losses, SPs in 2D materials can be observed just at low temperatures. These SPs lie in the mid-infrared (MIR) wavelength range [3]. Another 2D plasmonic material is graphene that has several advantages, such as high confinement, chemical doping or electrical gating tunability, low losses [11], and terahertz-to-MIR SPs [6, 12] at room temperatures.

SPs in graphene can be controlled by doping or electrical gating. The SP dispersion in graphene nanoribbons can be modified by varying their width [13–17]. In condensed-matter literature the plasmon modes of a system are obtained from the zeros of its dielectric function [18]. In 2D and 1D systems, such as graphene and its nanoribbons, *they become SPs*. The SP modes in a AGNR, schematically shown in Fig. 1, have been obtained *numerically* from the zeros of its dielectric function for zero and finite temperatures, as well as different geometries [13–17], only in the RPA approximation and usually without including screening and scattering. This approach cannot distinguish between TM and TE SP modes. Moreover, the quality factor of the SP field apparently has not been calculated.
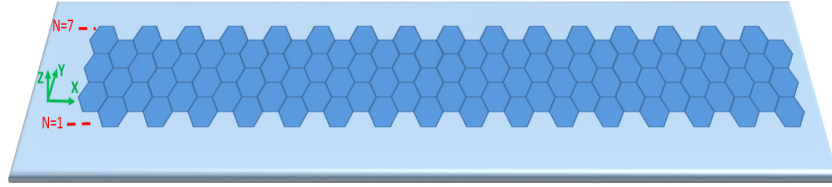

Fig. 1. Geometry of a AGNR.

The width of the nanoribbons and the type and quality of their edges determine whether they are metallic or semiconducting. The aforementioned studies [13–17, 19] and many others consider metallic nanoribbons but their existence has been seriously questioned by first-principle and tight-binding band-structure calculations [20] which find that they are semiconducting. Of course such a behaviour is found in nanoribbons created from graphene on a hBN substrate [21]. However, recent experimental studies reported both, (zero gap) metallic and (finite gap) semiconducting nanoribbons for widths as small as 4.5 nm [22].

In this work we evaluate the TM Lindhard, RPA, and Hubbard SPs in a metallic AGNR by satisfying the boundary conditions for the incoming, reflected, and transmitted EM fields that enter Maxwell's equations. In Sec. 2 we present the formalism, *analytic* dispersion relations (DRs) for each approach that include screening, and relate the SP field with the quality factor Q. We also include scattering by impurities in the long-wavelength limit. In Sec. 3 we present various numerical results and in Sec. 4 our summary. Some results are derived in appendices A-D.

2. Formalism

In this work we consider only AGNRs. A AGNR is surrounded by two media with permittivities ϵ_1 and ϵ_2, as shown in Fig. 2, in which the incident, reflected, and transmitted components of the light's electric field are shown. We assume that the two media have the same permeabilities $\mu_2 = \mu_1 = \mu_0$. By satisfying the boundary conditions for the normal ($\perp$) and tangential ($\parallel$) components of the field, Maxwell's equations lead to

$$\epsilon_1 E_1^\perp - \epsilon_2 E_2^\perp = \rho_s, \tag{1}$$

where ρ_s is surface charge density, and

$$E_1^{\parallel} - E_2^{\parallel} = 0. \tag{2}$$

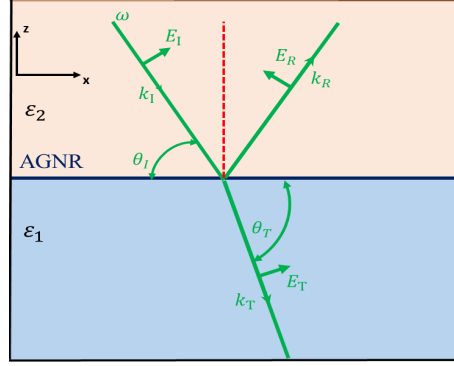As detailed in appendix A, combining Eqs. (1) and (2) with the continuity equation we obtain

Fig. 2. A AGNR at the interface of two media with permittivities ε_1 and ε_2.

the transmission t and reflection r amplitudes

$$t(k, \omega) = 2\left[\frac{n_1}{n_2} + \frac{\sin\theta_T}{\sin\theta_I} + \frac{\sin\theta_T}{n_2\varepsilon_0 c}\,\sigma(k,\omega)\right]^{-1} \tag{3}$$

$$r(k, \omega) = 1 - \frac{\sin\theta_T}{\sin\theta_I}\,t(k,\omega)\,; \tag{4}$$

here σ is the conductivity, $\epsilon_i = n_i^2\epsilon_0$, $i = 1, 2$, and n_i the refractive index. For low energies σ can be obtained from the continuity equation and the linear-response charge density, see appendix B, as

$$\sigma(q, \omega) = (iNe^2\omega/q^2)\,\chi(q,\omega), \tag{5}$$

where $\chi(q,\omega)$ and N are the polarization function and dimer respectively. This SP dispersion relation (DR) is obtained from the pole of the transmission or reflection amplitudes [23]. Now from Fig. 2 we readily have $\sin\theta_T = k_{1z}/k_1 = k_{1z}c/n_1\omega$ and $\sin\theta_I = k_{2z}/k_2 = k_{2z}c/n_2\omega$. Inserting these expressions in the denominator of Eq. (3), set equal to zero, and taking $k_{jz} \simeq ik_x$, cf. Eq. (C.2), leads to the DR [24]

$$q \simeq i\omega(\epsilon_1 + \epsilon_2)/\sigma(q,\omega). \tag{6}$$

This DR depends on whether the evaluation of $\sigma(q,\omega)$ includes scattering or not. Below we consider the two cases separately and show results without and with screening.

2.1. Absence of scattering

We consider surface plasmons with energy smaller that Fermi energy, that is, we consider only intraband transitions. Then for zero temperature, and $q \leq k_F$ the polarization function of a metallic AGNR, of width W, when the electron-electron interaction is neglected, is [17]

$$\chi^0(q, y, \omega) = -\frac{2}{Wh}\frac{v_F q^2}{v_F^2 q^2 - \omega^2}. \tag{7}$$

The Lindhard polarization is

$$\chi^{Lin}(q,\omega) = \chi^0(q,\omega) = \int_0^W \chi^0(q,y,\omega)dy, \tag{8}$$

A better approximation is the RPA which works very well for high electron densities. In it the Coulomb interaction changes the polarization function and gives

$$\chi^{RPA}(q,\omega) = \frac{\chi^0(q,\omega)}{1 - V(q)\chi^0(q,\omega)}, \tag{9}$$

Here $V(q)$ is the Fourier transform of the matrix element of the 2D screened Coulomb potential, with respect to x, $V(x,y) = e^{-k_s r}/r, r^2 = x^2 + y^2$,

$$V(q) = \frac{2e^2}{\epsilon_0} \int_0^1 \int_0^1 K_0[\delta_\lambda|(y - y')|]dydy', \tag{10}$$

where $\delta_\lambda = W(k_s^2 + q^2)^{1/2} = Wk_F(\lambda^2 + k_s'^2)^{1/2}, \lambda = q/k_F, k_s' = k_s/k_F$, and K_0 is the zeroth order modified Bessel function, see Eq. (4) on p. 495 of Ref. [25], and k_s measures the strength of screening. As a test, if we set $k_s = 0$ we obtain the usual $q \to 0$ logarithmic divergence.

If one takes into account the exchange interaction between electrons as well as correlation effects, the polarization function becomes more accurate. In this Hubbard approach one obtains

$$\chi^{Hub}(q,\omega) = \frac{\chi^0(q,\omega)}{1 - V(q)\left[1 - G(q)\right]\chi^0(q,\omega)}, \tag{11}$$

where $G(q)$ is the local field factor. For 1D systems $G(q)$ is given by [26]

$$G(q) = V((q^2 + k_F^2)^{1/2})/2V(q). \tag{12}$$

We plot $V(q)$ versus q/k_F in Fig. 3(a) for different k_s. As seen, $V(q)$ decreases with k_s but only for very small q, i.e., only in the long-wavelength limit, and is insensitive to k_s for $q/k_F \geq 0.2$. This behaviour is contrasted with the screened $V(q)$ for 2D graphene in panels (b) and (c): (b) is the RPA result, Eq. (2.23) of Ref. [27] with $1/q \to 1/\sqrt{q^2 + k_s^2}$ and $\epsilon = \epsilon_0 + (\pi/2)e^2/\hbar v_F$ the effective dielectric constant, while (c) is the Thomas-Fermi one, Eq. (2.23) of Ref. [27] with $V_{sc}^{TF}(q) = (1/\epsilon_0)(2\pi e^2/(q + q_{TF})$, $q_{TF} = 2\pi e^2 D(E_F)/\epsilon_0$ the Thomas-Fermi wave vector, and $D(E_F)$ the density of states at the Fermi level. If $D(E_F)$ is broadened due to scattering, q_{TF} can take several values depending on the level width γ. Notice that in (a) $q \equiv q_x$ whereas in (b) and (c) q is the 2D wave vector and $q'_{TF} \equiv q_{TF}/k_F$. Note also that for $k_s \to 0$, the results in (a) and (b) diverge for $q \to 0$.

The SP DRs are obtained by substituting Eq. (5) into Eq. (6) and by using $W = \sqrt{3}(N+1)a_{cc}/2$ with a_{cc} the carbon-carbon bond length. The results are

$$\hbar\omega/E_F = \sqrt{\lambda^2 + \zeta\lambda}, \qquad\qquad Lindhard, \tag{13}$$

$$\hbar\omega/E_F = \sqrt{\lambda^2(1 + \lambda\beta_\lambda) + \zeta\lambda}, \qquad RPA, \tag{14}$$

$$\hbar\omega/E_F = \sqrt{\lambda^2(1 + \lambda\gamma_\lambda) + \zeta\lambda}. \qquad Hubbard \tag{15}$$

Here $N = 3m - 1$, m is an integer,

$$\zeta = 2e^2/[\pi\sqrt{3}(\epsilon_1 + \epsilon_2)a_{cc}E_F](N/(N+1)) \tag{16}$$

$$\beta_\lambda = \frac{2e^2}{\hbar v_F \epsilon_0} \int_0^1 \int_0^1 K_0 [\delta_\lambda |(y - y')|] \, dy dy', \tag{17}$$

with $\gamma_\lambda = \beta_\lambda - 0.5\beta_{\chi'}$, and $\lambda' = (\sqrt{1 + \lambda^2})$. As a test, we expect that in the long-wavelength limit the SP DR becomes that of graphene [28] for W or N sufficiently large. Indeed, for N very large $N/(N + 1) \to 1$ and $\lambda \ll 1$ we have $\hbar\omega/E_F \propto \sqrt{\lambda}$ as in graphene's case [11, 28–32]. Furthermore, in the long-wavelength limit the SP field is proportional to $\zeta^{1/2}$ or $1/\sqrt{W}$ in line with expectations [33–35] and observations Ref [12, 36]. Another partial test is that Eq. (7) was also obtained from the collisionless Boltzmann equation.

2.2. Presence of scattering

For scattering by impurities the polarization function in the long-wavelength limit becomes [37]

$$\chi_{im}^0(q, \omega) = \frac{(1 - i\omega\tau) \, \chi^0(q, \omega + i\gamma)}{1 - i\omega\tau + [\chi^0(q, \omega + i\gamma)/\chi^0(q, 0) - 1]}, \tag{18}$$

with $\gamma = 1/\tau$ and τ the relaxation time. Then, as detailed in Appendix E, using Eqs. (5), (6), (18) and setting $\hbar\omega/E_F = \nu$, $\hbar\gamma/E_F = \gamma'$, and $S = \nu^2 + \gamma'^2$ we obtain the Lindhard DR

$$\lambda = [P_1 + \zeta^2 \sqrt{P_2}/2S]^{1/2}. \tag{19}$$

The polynomials of ν^2, P_1 and P_2, are given in Appendix E. Using the same procedure we obtain the RPA DR

$$\lambda = [P_4 + \sqrt{P_5}/2P_3]^{1/2}, \tag{20}$$

with P_3, P_4, and P_5 given in Appendix E. For the Hubbard DR we find Eq. (20) with β_λ changed to γ_λ. It is easy to verify that for $\gamma = 0$ Eqs. (19) and (20) reduce to Eqs. (13) and (14), respectively. Also, Eq. (20) gives Eq. (15) if we change β_λ to γ_λ and set $\gamma = 0$.

As indicated by Eq. (18), when scattering is present χ becomes complex and its imaginary part measures the plasmon strength [37]. We will consider only the RPA result in the long-wavelength limit. Then

$$\text{Im} \, \chi^{RPA} = \frac{\text{Im} \, \chi_{imp}^0}{\left[1 - V(q)\Re\chi_{imp}^0\right]^2 + \left[V(q)\text{Im} \, \chi_{imp}^0\right]^2} \tag{21}$$
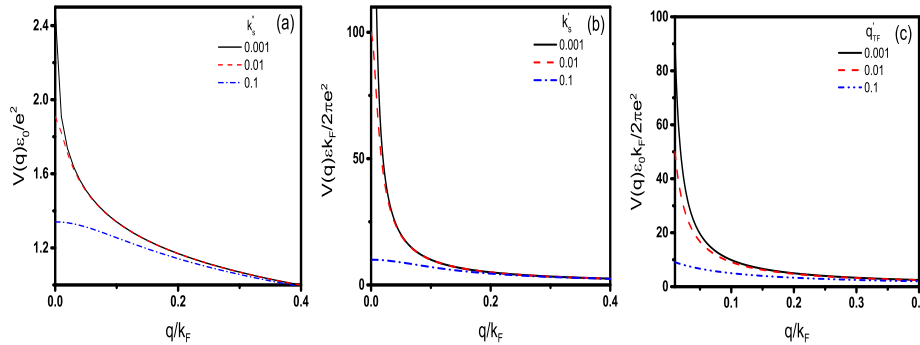

Fig. 3. Matrix element of the screened potential vs q/k_F in (a) a AGNR for $N = 14$, $E_F = 0.1$ eV, and 2D graphene in (b) the RPA and (c) Thomas-Fermi approaches.

is a measure of the plasmon strength that we will plot.

2.3. Transmission, reflection, and quality factor

The reflection coefficient is given by

$$R(\theta, \omega) = (1 - \delta_{\theta, \theta_B}) |r|^2, \tag{22}$$

with θ the angle of incidence and θ_B the Brewster angle. When the phase matching condition is satisfied for SPs, the transmission amplitude becomes (see appendix C)

$$t \sim 4Q^2/r_n, \tag{23}$$

where $r_n = (n_1^2 + n_2^2)/n_1 n_2$ and Q is the quality factor defined by $Q = \Re q / \operatorname{Im} q$. Then the SP field becomes

$$E_{SP} \sim 4Q^2 E_I/r_n, \tag{24}$$

with E_I the amplitude of $\vec{E}_I$ shown in Fig. 2.

3. Numerical results

We first present results without including screening and scattering. In Fig. 4 we plot the Lindhard and Hubbard TM SP DRs for different widths ($N = 5, 8, 20$) of a metallic AGNR, with $n_1 = 2, n_2 = 1$, and $E_F = 0.1$ eV. For fixed energy, especially in the long-wavelength limit, the SP wavelength increases with the width W of the AGNR and so does the SP group velocity. The opposite occurs when W is decreased. The RPA result is similar to the fully numerical ones of Refs. [13–16].
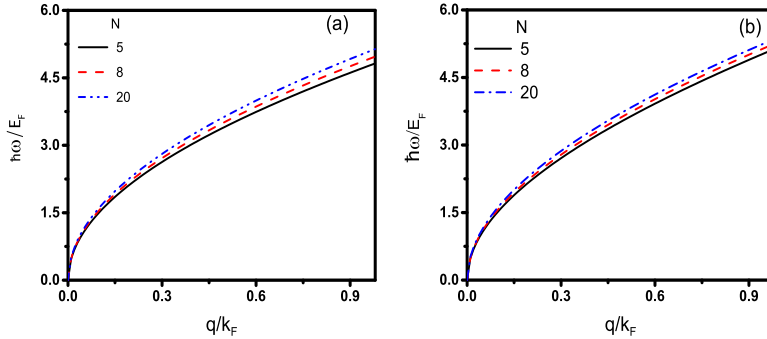

Fig. 4. (a) TM Lindhard and (b) Hubbard SP DRs in a metallic AGNR with $n_1 = 2, n_2 = 1$, and $E_F = 0.1$ eV. From top to bottom the AGNR width is $N = 5, 8, 20$.

The N dependence shown in Fig. 4 can be understood as follows. The energy of a system in a EM field is directly related to the induced polarization which leads to a charge density oscillation. The polarization can be considered as an ensemble of dipole moments (DMs). For an oscillation with specific displacement from equilibrium, by increasing the number of DMs, which in a AGNR is proportional to the width W (or the dimmer number N), the generated EM field has more energy. Therefore, we expect that, as shown in Fig. 4, its frequency or photon energy to increase with the AGNR width W.

In Fig. 5 we contrast the TM Lindhard, RPA, and Hubbard SP dispersions for N = 8. As the inset shows, even in the long-wavelength limit there is a small but noticeable difference between them.

The difference between the DRs shown in Fig. 5 can be understood as follows. The strength of the charge displacement/polarization due to a EM field is reduced when, e.g., we take into account electron-electron interaction and go from Eq. (8) to Eq. (9) and subsequently to Eq. (11) upon including exchange. To have the same polarization, which determines the SP photon energy, as in the case without electron-electron interaction, the charge displacement must be increased. Then the uncertainty principle indicates that the modified momentum ($\propto q$) is smaller. In addition, from photon energy conservation one can conclude that for a specific SP mode its intensity in the Lindhard case is stronger than in Hubbard and RPA cases because of the SP wavelength increase in the former case as compared to the latter ones.

We now turn to the conductivity given by Eq. (5). *In the absence of scattering* we use Eqs. (5), (7) and (8) for $\chi^0(q, \omega)$, and plot it in Fig. 6. The three "lines" shown in the contour plots follow the roots of the denominators in $\chi(q, \omega)$. We also see that the slope of the Lindhard case increases as we move to the Hubbard and RPA results. This reflects the change in the denominators of χ due to the factors $V(q)$ and $G(q)$ in Eqs. (9) and (11). To better appreciate the differences between the three approaches we plot cross sections of Fig. 6 in Fig. 7(a) for fixed $q/k_F = 0.18$ and in Fig. 7(b) for fixed $\hbar\omega/E_F = 0.48$. The dependence of the Hubbard conductivity on the width of the AGNR is shown in Fig. 8 for widths $N = 8, 14, 20$. As seen, the dips move to the right with increasing N. However, we cannot increase N indefinitely because the 1D potential $V(q)$, given by Eq. (10), is less and less valid for increasing N. The results in Figs. 4-8 do not include screening and one may wonder how much they change when screening is included. The answer is that, apart from the removal of the logarithmic divergence for $q \to 0$, the DRs and Fig. 6 change very little, the changes are not visible on the scales used. More substantial changes occur in the plasmon strength, see below.

In the presence of scattering the conductivity has a real and an imaginary part. In Fig. 9 we plot its magnitude, in the long-wavelength limit, for $N = 14$ and $E_F = 0.1$ eV.

The top panels are for $\gamma' = 0$, the middle ones for $\gamma' = 0.001$, and the bottom panels for $\gamma' = 0.03$. As seen, increasing the scattering strength γ, drastically changes its magnitude especially for the right part of the panels in the third row. At the same time we see that increasing γ reduces the slopes of the straight "lines" in Fig. 6 and slightly shortens the $\hbar\omega/E_F$ regions of maximal conductivity.

Regarding the plasmon strength we present, in Fig. 10, a (ω, q) contour plot of $-\pi\hbar v_F \text{Im} \chi^{RPA}$. On the first row the three panels are for $\gamma' = 0.001, 0.005, 0.009$, respectively, and screening is neglected. On the second one screening is included and the panels are for $\gamma' = 0.001$, and $k'_s = 0.001, 0.01, 0.1$., respectively.
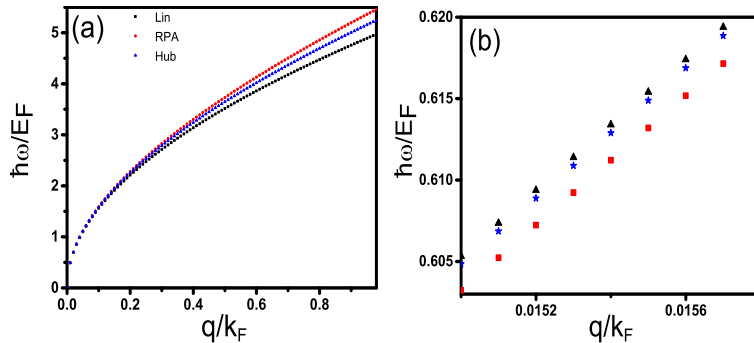

Fig. 5. TM Lindhard, RPA, and Hubbard SP dispersions in a AGNR for $E_F = 0.1$ eV and width $N = 8$ for (a) $q/k_F \leq 1$ and (b) long wavelength limit, $q/k_F \to 0$.
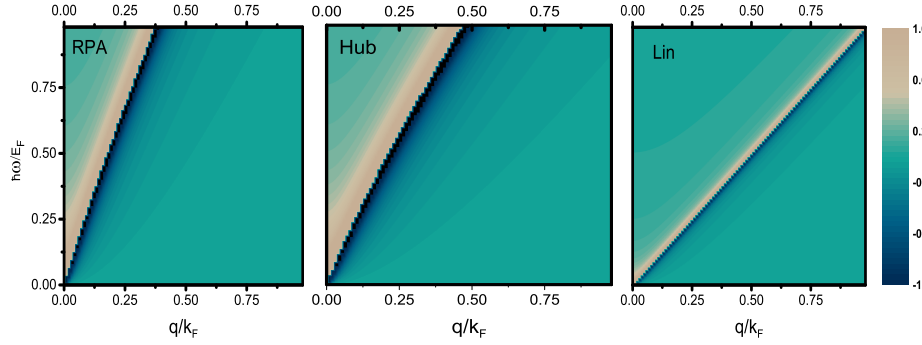
Fig. 6. (ω, q) contour plot of the RPA, Hubbard, and Lindhard conductivities of a metallic AGNR for $N = 14$ and $E_F = 0.1$ eV.
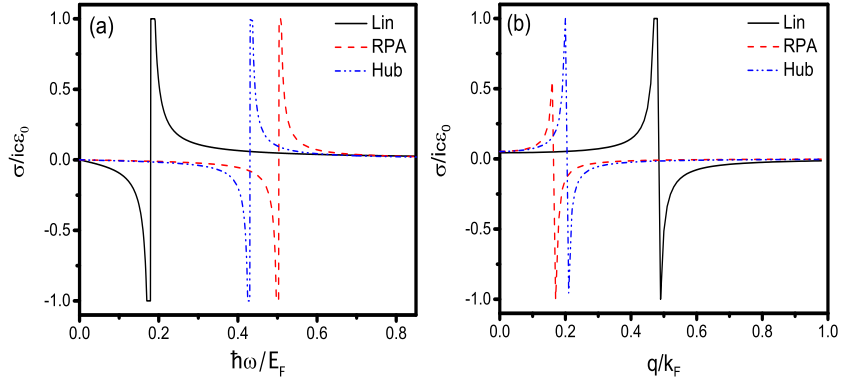

Fig. 7. Cross sections of Fig. 6 for (a) $q/k_F = 0.18$ and (b) $\hbar\omega/E_F = 0.48$.
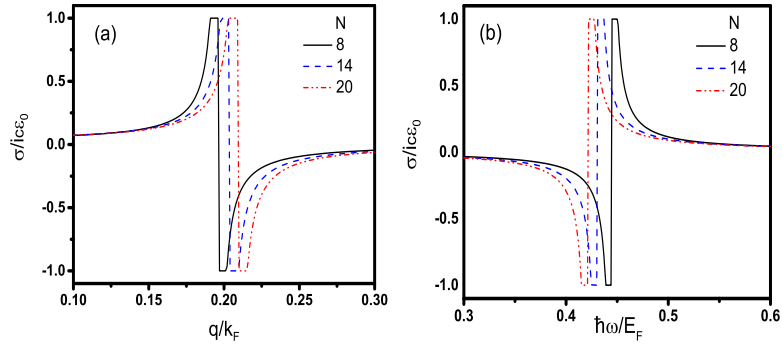

Fig. 8. Hubbard conductivity for $N = 8, 14, 20$ and $E_F = 0.1$ eV. Panel (a) is for fixed $\hbar\omega/E_F = 0.48$ and panel (b) for fixed $q/k_F = 0.18$.
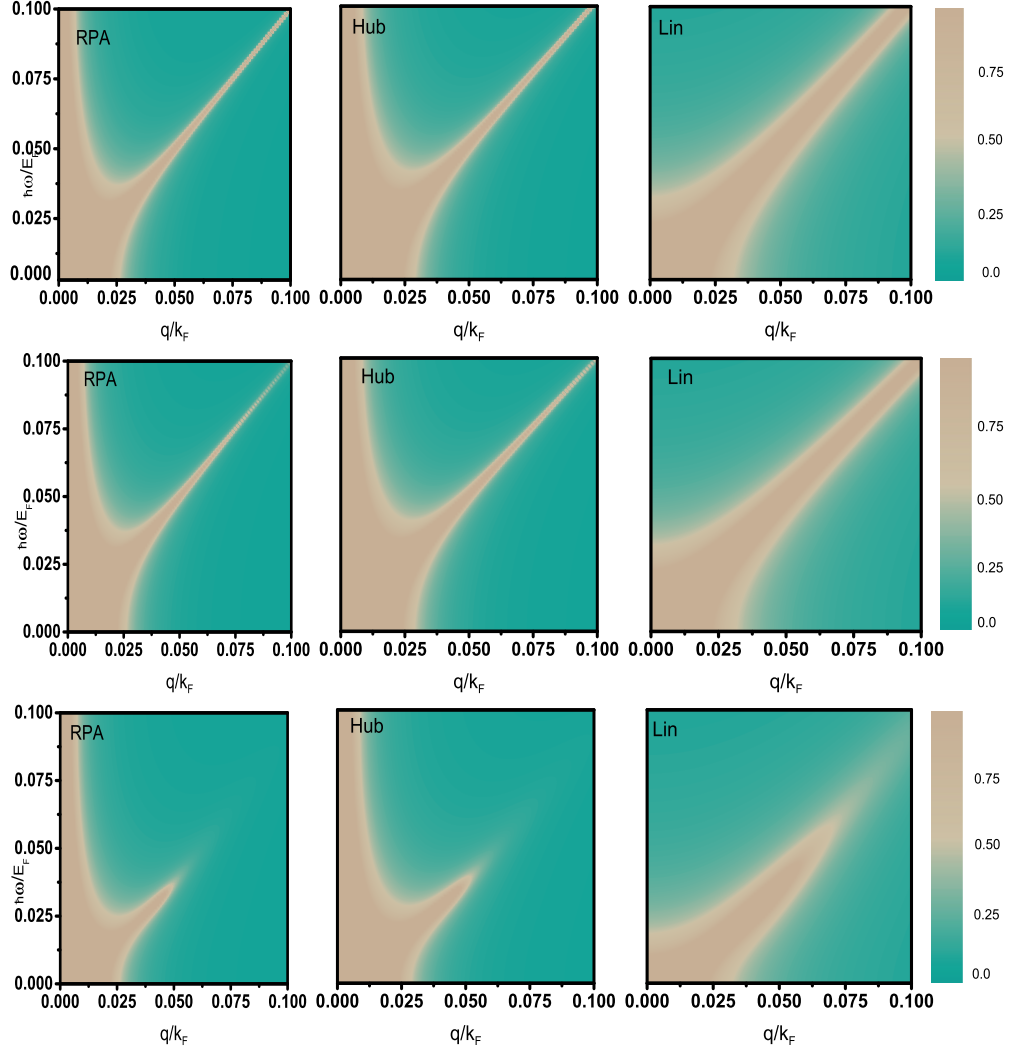
Fig. 9. (ω, q) amplitude contour plot of the RPA, Hubbard, and Lindhard conductivities of a metallic AGNR, in the long-wavelength limit, for $N = 14$ and $E_F = 0.1$ eV. The top panels are for $\gamma' = 0$, the middle ones for $\gamma' = 0.001$, and the bottom panels for $\gamma' = 0.03$.
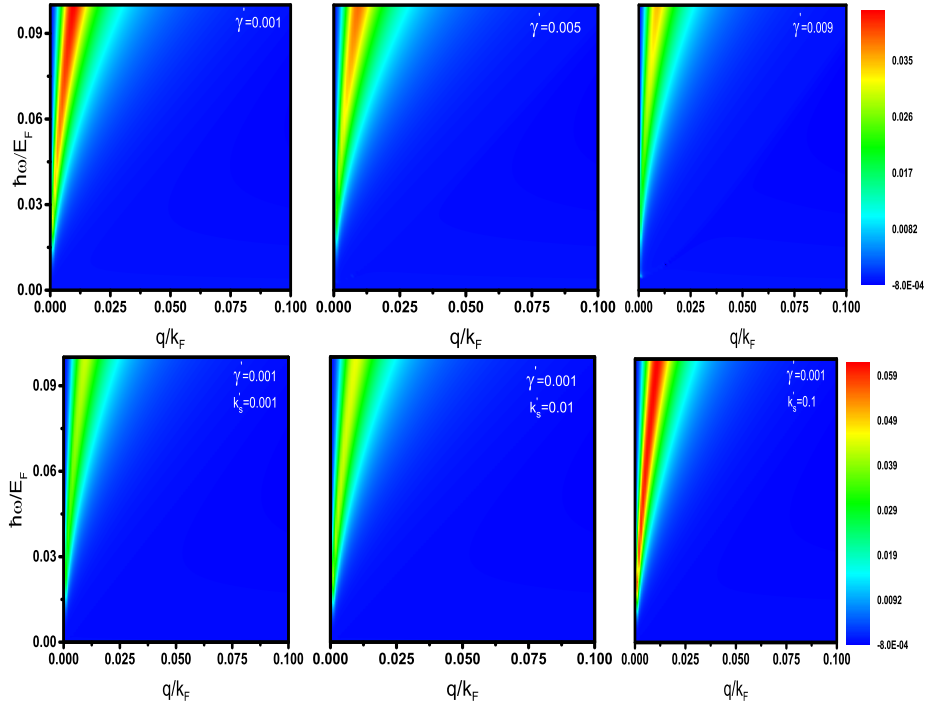
Fig. 10. (ω, q) contour plot of $-\pi\hbar v_F \operatorname{Im} \chi^{RPA}$ for a metallic AGNR with $N = 14$ and $E_F = 0.1$ eV. The first row of panels is for an *unscreened* potential with $\gamma' = 0.001, 0.005$, and 0.009., the second row for a *screened* one with $\gamma' = 0.001$ and $k'_s = 0.001, 0.01, 0.1$..

In the experiments when phase matching occurs, for a fixed frequency the wave vector of the incoming field is the same as the SP, the reflected field that reaches the detector, which measures its coefficient, vanishes. It also vanishes at the Brewster angle.

In Fig. 11(a) we plot the RPA reflection coefficient R, given by Eq. (22) versus the angle of incidence θ for $N = 14$, $E_F = 0.1$ eV, $n_1 = 2$ and $n_2 = 1$ in the absence of screening and scattering. A cross section of this graph for $\hbar\omega/E_F = 0.5$ is shown in Fig. 11(b) together with the 2D substrate result (dot-dashed blue curve) which shows that the substrate supports Brewster angles. Notice that the two results differ drastically and that there is no Brewster angle in a AGNR. This means that, e.g., in the Kretschmann geometry, if the detector shows a zero value the SP has been launched.

Graphene itself supports both TM and TE modes. However, AGNR nanoribbons support only TM modes, there is no TE mode (see appendix D). This suggests the application of a suspended AGNR as a TM polarizer.
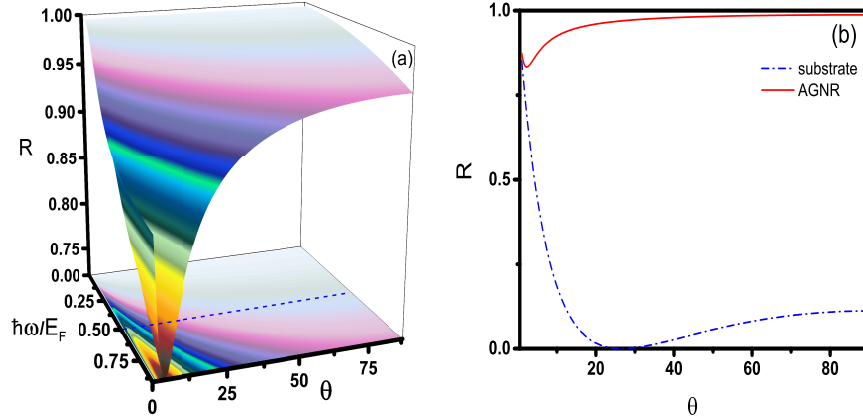
Fig. 11. (a) RPA Reflection coefficient for $N = 14$, $E_F = 0.1$ eV, $n_1 = 2$ and $n_2 = 1$ in the absence of screening and scattering. (b) The solid red curve is a cross section of (a) for $\hbar\omega/E_F = 0.5$ and the dot-dashed blue one the result for a 2D substrate.

4. Summary

We investigated SPs in AGNRs following the Lindhard, random-phase approximation (RPA), and Hubbard approaches. For TM modes we obtained analytical DRs valid for $q \leq k_F$ and assessed their width dependence. In addition, we included screening using a Yukawa-type potential; the results though, apart from those in the long-wavelength limit $q \to 0$ are not drastically affected. We also rederived these DRs for scattering by impurities in the long-wavelength limit and highlighted the differences in the conductivity magnitudes, in the three approaches, with increasing scattering strength. In this limit scattering can drastically modify the respective, scattering-free conductivities. Further, we showed that the SP field is proportional to the square of the quality factor Q. For TE modes the pole of the reflection amplitude shows that AGNRs do not support TE SPs. Also, AGNRs do not support Brewster angles.

Appendices

A. TM transmission and reflection amplitudes

Written explicitly in terms of the field amplitudes and angles of incidence θ_I, transmission θ_T, and refraction θ_R, Eqs. (1) and (2) take the form

$$\epsilon_2(E_I \cos\theta_I + E_R \cos\theta_R) - \epsilon_1 E_T \cos\theta_T = \rho_s, \tag{A.1}$$

$$(E_I \sin\theta_I - E_R \sin\theta_R) - E_T \sin\theta_T = 0. \tag{A.2}$$

Fourier transforming the continuity equation gives

$$-\omega\rho_s(q,\omega) + k_x J_x(q,\omega) = 0, \tag{A.3}$$

where $k_x = k_T \cos\theta_T$. Setting

$$J_x(q,\omega) = \sigma(q,\omega)E_x(q,\omega), \tag{A.4}$$

and noticing $E_x(q, \omega) = E_T(q, \omega) \sin \theta_T$ gives

$$\rho_s(q, \omega) = [\sigma(q, \omega)/\omega] k_T E_T \sin 2\theta_T / 2. \tag{A.5}$$

We now use Snell's law $n_2 \cos \theta_I = n_1 \cos \theta_T, \theta_I = \theta_R$, and write $E_R = rE_I$, $E_T = tE_I$. Furthermore, we have $\epsilon_1/\epsilon_2 = n_1^2/n_2^2$, $k_T = n_1\omega/c$, and $\epsilon_i/\epsilon_0 = n_i^2$. Then Eqs. (A.1) and (A.2) become

$$(1 + r) \cos \theta_I = (\epsilon_1 + [\sigma(q, \omega)/\omega] k_T \sin \theta_T) t \cos \theta_T / \epsilon_2, \tag{A.6}$$

$$(1 - r) \sin \theta_I = t \sin \theta_T. \tag{A.7}$$

Solving Eqs. (A.6) and (A.7) for r and t gives Eqs. (3) and (4) of Sec. II.

B. Conductivity

The surface charge density ρ_s can be expressed as

$$\begin{aligned}
\rho_s(\vec{x}, t) &= \sum_{i=1}^{N} \int \int \rho(x, y, z, t) \delta(y - y_i) \delta(z) dy dz \\
&= N\rho(x, t),
\end{aligned} \tag{B.1}$$

where N is the dimer number. Then the Fourier transform of the continuity equation is given by Eq. (A.3) with $\rho_s(k, \omega) = N\rho(k, \omega)$. We now use Eq. (A.4) for the current density J, write the electric field E in terms of the external potential Φ_{ext},

$$E(k, \omega) = -\nabla \phi(k, \omega) = -i\vec{k}\phi_{ext}(k, \omega), \tag{B.2}$$

and substitute these expressions in the general form [18]

$$\rho(k, \omega) = e^2 \chi(k, \omega)\phi_{ext}(k, \omega). \tag{B.3}$$

Then Eqs. (A.3), (B.2), and (B.3) give the conductivity in the form of Eq. (5).

C. Transmission amplitude, quality factor

Expressed in terms of wave vectors, with the help of Fig. 2, the denominator in Eq. (3) becomes

$$\frac{n_1}{n_2} + \frac{k_{2z}n_2}{k_{1z}n_1} + \frac{k_{2z}}{n_1 n_2 \varepsilon_0} \frac{\sigma(k, \omega)}{\omega}, \tag{C.1}$$

where $k_{jz} = i[k_x^2 - k_j^2]^{1/2}$, $j = 1, 2$, and

$$k_{jz} = i|k_x|[1 - (k_j/k_x)^2]^{1/2} \simeq i|k_x|, \tag{C.2}$$

since, after the surface plasmon is launched, we have $k_x \equiv k_{sp}$ and $k_j/k_x \ll 1$. Because the surface plasmon will be damped after a distance, its wave vector has a damping term that we denote by k_{Ix}. Then Eq. (C.2) becomes

$$|k_x| = [k_{Rx}^2 + k_{Ix}^2]^{1/2} = k_{Rx}[1 + Q^{-2}]^{1/2}, \tag{C.3}$$

where $Q = \Re q / \mathrm{Im}\, q$ is the quality factor. Using Eq. (C.3), $|k_x| = \omega\epsilon_0(n_1^2 + n_2^2)/\sigma(k, \omega)$, and the approximation $1 - [1 + Q^{-2}]^{1/2} \approx Q^{-2}/2$ gives the transmission amplitude, when the phase matching condition for launching surface plasmons occurs, in the form $(r_n = (n_1^2 + n_2^2)/n_1 n_2)$

$$t(k, \omega) \sim 4 Q^2/r_n, \tag{C.4}$$

with $Q = \omega\tau = \omega/\gamma$ and τ the relaxation time.

D. TE transmission and reflection amplitudes

By satisfying the boundary conditions for the normal and tangential components of the magnetic field B in Maxwell's equations, see Fig. 2 with the electric field E replaced by $B = \mu H$, the tangential components give

$$H_2^{||} - H_1^{||} = \vec{k}_f \times \hat{n}, \tag{D.1}$$

with $\vec{k}_f$ the vector of free surface current, and the normal components

$$B_2^{\perp} - B_1^{\perp} = 0. \tag{D.2}$$

For simplicity we assume $\mu_1 = \mu_2 = \mu_0$. Also, $\theta_I = \theta_R$ and $n_2 \cos\theta_T = n_1 \cos\theta_I$. Then Eqs. (D.1) and (D.2) are first rewritten in terms of B_I, B_R, and B_T, similar to Eqs. (A.1) and (A.2), and then in terms of the refractive indices like Eqs. (A.6) and (A.7). The result is

$$1 - r = t \left(\frac{n_2}{n_1} + \frac{\sigma_{yy}}{n_1 \epsilon_0 \sin\theta_T} \right) \frac{\sin\theta_T}{\sin\theta_I}, \tag{D.3}$$

$$1 + r = t. \tag{D.4}$$

From Eqs (D.3) and (D.4) we readily obtain

$$t = 2 \left[1 + \left(\frac{n_2}{n_1} + \frac{\sigma_{yy}}{n_1 \epsilon_0 \sin\theta_T} \right) \frac{\sin\theta_T}{\sin\theta_I} \right]^{-1}. \tag{D.5}$$

For graphene nanoribbons we have $\sigma_{yy} = 0$. Then, as proven in [5], Maier, the pole of the transmission amplitude does not lend any support to TE surface plasmons.

E. DRs in the presence of scattering

For scattering by impurities the polarization function in the long-wavelength limit is given by Eq. (18). Then using Eqs. (5), (6), (18) and setting $\hbar\omega/E_F = \nu$ and $\hbar\gamma/E_F = \gamma'$ we obtain the Lindhard SP DR by solving

$$\lambda^2 \zeta^2 S = \nu^2 (S - \lambda^2)^2 + \gamma'^2 \left(2\nu^2 - \lambda^2 \right)^2, \tag{E.1}$$

with $S = \nu^2 + \gamma'^2$, for λ^2 or ν^2. Equation (E.1) is quadratic in λ^2 but cubic in ν^2. Solving it for λ^2, $\lambda = q/k_F$, we find Eq. (19) with

$$P_1 = \left[3\gamma'^2 \nu^2 + S/2\zeta^2 + \nu^4 \right] / S \tag{E.2}$$

$$P_2 = S^2 + 4\nu^2 (S + 2\gamma'^2)[\gamma'^2(S - 2\gamma'^2)/\zeta^2 + S]/\zeta^2. \tag{E.3}$$

Using the same procedure we obtain the RPA DR

$$\lambda^2 \zeta^2 S = (S - \lambda^2)^2 + \gamma'^2 \left[2\nu^2 - \lambda^2 \left(1 + \beta_\lambda \right) \right]^2. \tag{E.4}$$

The solution is Eq. (20) with P_3, P_4, and P_5 given by

$$P_3 = [S(1 + \beta_\lambda^2) + 2\beta_\lambda \gamma'^2 (1 + \nu^2)]/\zeta^2, \tag{E.5}$$

$$P_4 = \left[\nu^2 (S + 2\gamma'^2)(1 + \beta_\lambda) + S\zeta^2 \right] / 2\zeta^2, \tag{E.6}$$

$$P_5 = 4P_4^2 - 4P_3 \nu^2 (S^2 + 4\gamma'^2 \nu^2)/\zeta^2, \tag{E.7}$$

respectively. For the Hubbard dispersion we find Eq. (19) with β_λ changed to γ_λ.

Acknowledgments